

AD-A201 698

REF. FILE COPY

(4)

AFGL-TR-88-0149

Advanced Computational Techniques in
Regional Wave Studies

R. B. Herrmann
T. A. Mokhtar
D. R. Russell

St. Louis University
Department of Earth and
Atmospheric Sciences
St Louis, MO 63156-8099

17 June 1988

Scientific Report No. 1

APPROVED FOR PUBLIC RELEASE; DISTRIBUTION UNLIMITED

AIR FORCE GEOPHYSICS LABORATORY
AIR FORCE SYSTEMS COMMAND
UNITED STATES AIR FORCE
HANSCOM AIR FORCE BASE, MASSACHUSETTS 01731-5000

DTIC
ELECTE
OCT 31 1988
S D
E

88 10 28 06 8

UNCLASSIFIED

SECURITY CLASSIFICATION OF THIS PAGE

REPORT DOCUMENTATION PAGE

1a. REPORT SECURITY CLASSIFICATION UNCLASSIFIED		1b. RESTRICTIVE MARKINGS	
2a. SECURITY CLASSIFICATION AUTHORITY		3. DISTRIBUTION/AVAILABILITY OF REPORT Approved for public release, distribution unlimited.	
2b. DECLASSIFICATION/DOWNGRADING SCHEDULE		4. PERFORMING ORGANIZATION REPORT NUMBER(S)	
4. PERFORMING ORGANIZATION REPORT NUMBER(S)		5. MONITORING ORGANIZATION REPORT NUMBER(S) AFGL-TR-88-0149	
6a. NAME OF PERFORMING ORGANIZATION Saint Louis University	6b. OFFICE SYMBOL (If applicable)	7a. NAME OF MONITORING ORGANIZATION Air Force Geophysics Laboratory	
6c. ADDRESS (City, State and ZIP Code) Department of Earth & Atmospheric Sciences St. Louis, MO 63156-8099		7b. ADDRESS (City, State and ZIP Code) Hanscom Air Force Base, MA 01731-5000	
8a. NAME OF FUNDING, SPONSORING ORGANIZATION DARPA	8b. OFFICE SYMBOL (If applicable)	9. PROCUREMENT INSTRUMENT IDENTIFICATION NUMBER F19628-87-K-0047	
8c. ADDRESS (City, State and ZIP Code) 1400 Wilson Boulevard Arlington, VA 22209		10. SOURCE OF FUNDING NOS.	
11. TITLE (Include Security Classification) Advanced Computational Techniques in Regional Wave Studies		PROGRAM ELEMENT NO. 611010E	PROJECT NO. 7A10
12. PERSONAL AUTHOR(S) R. B. Herrmann, T. A. Mokhtar* and D. R. Russell		TASK NO. DA	WORK UNIT NO. CO
13a. TYPE OF REPORT Scientific No. 1	13b. TIME COVERED FROM 1 JUN 87 to 31 May 88	14. DATE OF REPORT (Yr., Mo., Day) 1988 JUN 17	15. PAGE COUNT 52
16. SUPPLEMENTARY NOTATION *King Abdulaziz University, P. O. Box 1744, Jeddah, Saudi Arabia 21441			
17. COSATI CODES		18. SUBJECT TERMS (Continue on reverse if necessary and identify by block number)	
FIELD	GROUP	SUB. GR.	Surface wave; Shear velocity; Arabian shield. <i>101e</i> <i>Direct Data Transfer</i>
19. ABSTRACT (Continue on reverse if necessary and identify by block number)			
<p>→ The research performed under the contract during this period was directed toward verification of computational codes developed for surface-wave analysis. A high frequency data set obtained during a refraction experiment across the Arabian shield was used to obtain shallow shear wave velocity and Q. Low shear wave Q values were obtained in the upper 500 meters of the shield. The inverted model succeeds very well in matching observed waveforms in their entirety.</p> <p>A distribution of computer software, Computer Programs in Seismology, has been installed for use by researchers at the Center for Seismic Studies. These codes provide unique capabilities for work with regional seismic phases and surface waves. <i>Keywords:</i></p>			
20. DISTRIBUTION/AVAILABILITY OF ABSTRACT UNCLASSIFIED/UNLIMITED <input type="checkbox"/> SAME AS RPT. <input checked="" type="checkbox"/> DTIC USERS <input type="checkbox"/>		21. ABSTRACT SECURITY CLASSIFICATION UNCLASSIFIED	
22a. NAME OF RESPONSIBLE INDIVIDUAL James Lewkowicz		22b. TELEPHONE NUMBER (Include Area Code) (617)377-3028	22c. OFFICE SYMBOL AFGL/LWH

DD FORM 1473, 83 APR

EDITION OF 1 JAN 73 IS OBSOLETE.

UNCLASSIFIED
SECURITY CLASSIFICATION OF THIS PAGE

SUMMARY

The research performed under the contract during this period was directed toward the verification of computational codes developed for surface-wave analysis. A high frequency data set obtained during a refraction experiment across the Arabian shield was used to obtain shallow shear wave velocity and Q. Low shear wave Q values were obtained in the upper 500 meters of the shield. The inverted model succeeds very well in matching observed waveforms in their entirety.

A distribution of computer software, Computer Programs in Seismology, has been installed for use by researchers at the Center for Seismic Studies. These codes provide unique capabilities for work with regional seismic phases and surface waves.

Accession For	
NTIS GRA&I	<input checked="" type="checkbox"/>
DTIC TAB	<input type="checkbox"/>
Unannounced	<input type="checkbox"/>
Justification	
By _____	
Distribution/	
Availability Codes	
Dist	Avail and/or Special
A-1	



CONTENTS

SEISMIC VELOCITY AND Q MODEL FOR THE SHALLOW STRUCTURE OF THE ARABIAN SHIELD FROM SHORT PERIOD RAYLEIGH WAVES

Introduction	1
Geology Along the Profiles Used	3
Data	4
Method of Analysis	4
Phase velocity determination	5
Group velocity and anelastic attenuation	6
Inversion for Shear Velocity and Q_β	8
Waveform Modeling	11
Conclusion	14
Acknowledgments	16
References	16
List of Figures	19
COMPUTER PROGRAMS IN SEISMOLOGY	32

SEISMIC VELOCITY AND Q_β MODEL FOR THE SHALLOW STRUCTURE OF THE ARABIAN SHIELD FROM SHORT PERIOD RAYLEIGH WAVES

T. A. Mokhtar*, R. B. Herrmann‡, and D. R. Russell‡

ABSTRACT

The shear velocity and Q_β structure for the upper 1 km in different tectonic regions of the Arabian shield has been investigated using high frequency vertical component records of Rayleigh waves (1-20 Hz), which were recorded to distances of 55-80 km during a deep seismic refraction survey. The group and phase velocities of the fundamental and first higher modes were inverted for the shear wave velocity structure. The Rayleigh-wave attenuation coefficients were determined from the decay of the amplitude spectrum of the fundamental mode and used to invert for the Q_β structure. These models were tested by calculating synthetic seismograms for the fundamental and the first higher modes using surface-wave theory. A center of compression was used to represent the source, and both step and Dirac delta source time functions were tested. Modeling indicates that the shear wave velocity of the shield increases from 2.6 km/s to 3.4 km/s in the upper 400 m of the crust. Q_β increases from 30 in the upper 50 m to 150 at 500 m depth. The underlying material has a Q_β of 400-500 for the outcropping igneous rocks such as granite and may reach values higher than 700 for the metamorphic green schist rock. A Dirac delta source time function produces the best fit with observations.

INTRODUCTION

In February 1978, the United States Geological Survey in collaboration with the

* Faculty of Earth Sciences, King Abdulaziz University, P. O. Box 1744, Jeddah, Saudi Arabia 21441

‡ Department of Earth and Atmospheric Sciences, Saint Louis University, P. O. Box 8099 - Laclede Station, Saint Louis, Missouri 63156, U.S.A.

Directorate General of Mineral Resources of Saudi Arabia recorded a deep seismic refraction profile along a 1000 km line that traverses the Arabian shield. The seismic line begins in the mesozoic cover rocks in the northeast, continues to the southwest across the shield, and terminates at the outer edge of the Farasan Island in the southern Red Sea (Figure 1a). Using two dimensional ray tracing techniques in the data analysis, the recorded data were modeled primarily with horizontal layers (Healy et al., 1982; Mooney et al., 1985). The results indicate that the shield consists of two crustal layers, each about 20 km thick, with average compressional velocities of 6.3 km/s and 7 km/s for the upper and lower crust, respectively. The depth of the Moho discontinuity beneath the shield varies from 43 km in the northeast to 38 km in the southwest. The upper mantle velocity is 8.2 km/s in the northeast and decreases to 8.0 km/s in the southwest.

Surface wave signals have been extensively used to determine the velocity structure of the crust and the upper mantle in many regions of the earth (e.g, Kovach, 1978; Knopoff, 1972). Previous surface wave studies of the Arabian shield have been limited to very few paths and long periods, using Rayleigh waves generated by earthquakes (Niazi, 1968; Knopoff and Fouda, 1975). Shear-wave velocity models from these studies show a pronounced low velocity zone, the top of which is at a depth of 100-140 km. The phase velocities of the Arabian shield are lower than those of the Canadian shield; however, they are higher than those of the United States Gulf Coastal plain.

Studies that use surface waves from near explosion sources to investigate the properties in the upper crust are not very common. Al-Husseini et al. (1981) studied the dispersion patterns of ground roll in northeastern Saudi Arabia. They analyzed observations of high frequency Rayleigh waves (10-80 Hz) from exploration data, supplemented with geologic information as well as bore hole measurements of P-wave velocities, to produce maps of the distribution of minimum and maximum phase velocities of the Rayleigh waves in the region for use in group array design for reflection studies in an area northeast of the refraction profile.

The USGS seismic line displays high quality, coherent, dispersed short period Rayleigh waves which were recorded on record sections from several shot points to distances of 55-80 km. The signals can provide information on the elastic and anelastic properties of the upper portions of the crust. The purpose of this paper is to analyze the recorded short period Rayleigh waves to determine the properties of the shallow regions of the upper crust in the different tectonic provinces of the shield.

GEOLOGY ALONG THE PROFILES USED

The refraction profile traverses three major tectonic provinces in the Arabian Shield. Greenwood et al. (1980) suggested that the northwest trending Najd fault system divides the Precambrian shield into the Shammar, the Najd, and the Hijaz-Asir tectonic provinces. Of the 19 shots that were fired, three were detonated and recorded within these 3 provinces. These were at Shot Point 2 (SP2) in the Shammar province, at Shot Point 3 (SP3) in Najd province, and at Shot Point 4 (SP4) in the Hijaz-Asir province (see Figure 1a).

The Arabian shield has a complex geological history and composition. It consists predominantly of Precambrian crystalline rocks which are bounded to the east by a Phanerozoic sedimentary cover (Brown and Jackson, 1979). The shield is considered to have been formed from island arcs of west dipping subduction zones that were shifted successively to the east (Schmidt et al., 1978). Since we are concerned with limited portions of the shield, only a brief description of the geology of the areas where the seismic traces were used is given here. This description is taken primarily from Healy et al. (1982), Brown and Jackson (1979), and Greenwood et al. (1980).

Figure 1b shows an approximately 1 km thick geological cross section inferred from surface geology. The profile immediately northeast of SP2 traverses regions that are composed of andesite and granite gneiss, followed by the Abt schist formation in the region of the Al Amar-Idsas fault. This fault is a suture zone that extends north-northeast in an arc that is truncated at both ends by the northern boundary of the

shield. To the southwest of SP2, the crust is composed of andesitic rocks of the Halaban formation for a distance of 30 km where it contacts the Murdama formation, composed of basal conglomerate containing clasts of rhyolite, andesite, and granite. The Murdama formation is followed by granite and granite gneiss. To the northeast of SP3, the region consists of calc-alkaline granite that is bordered by the andesite rocks of the Halaban formation at about 40 km to the northeast. The granite continues to the southwest of SP3 to about 20 km where it is again bounded by the Halaban formation andesite. SP4 was detonated in granite, while the material adjacent to it, on both sides of the shot point, is carbonaceous and graphitic schist of the Hali schist formation. There is a greenschist unit 10 km southwest of SP4 that is composed of metaandesitic and metabasaltic schist and forms the remainder of the profile. To the northeast, the Hali schist is bordered by alkaline granite that alternates with units of greenschist facies.

DATA

Each data trace consists of 20 seconds of digital data with a sampling interval of 5 milliseconds. Standard 2 Hz vertical geophones were used. The signal was recorded using an analog recording instrument and was digitized subsequently. The traces were corrected for instrument response before processing to make ground velocity time histories. All seismic traces from the three shot points that show the fundamental mode Rayleigh waves were used in the analysis. These are the traces of SP2 at the locations 268-343 (Figure 2), traces of SP3 at the locations 378-438 (Figure 3), and traces of shot number SP4 at the locations 482-558 (Figure 4). In most cases, all traces from a given side of a shot point were used to obtain an average velocity structure for that side. Thus, small lateral heterogeneities were averaged, leading to one dimensional shear velocity models. In the case of the profile northeast of SP2, where Rayleigh waves at larger distances (locations 268-281) displayed a very different dispersion than those at shorter distances, two models were obtained.

METHOD OF ANALYSIS

The data required for inversion are the values of phase velocity, group velocity and anelastic attenuation as a function of frequency and surface-wave mode.

Phase velocity determination

McMechan and Yedlin (1981) described a method to obtain phase velocity from a dispersed wave in a common-shot wave gather. The method consists of performing a slant stack on the data to obtain a wave field in the $p-\tau$ domain (phase slowness-intercept time) followed by a one dimensional Fourier transform over τ to present the wavefield in the $p-\omega$ plane. The $p-\omega$ stack of a multi-mode surface wave can be written as

$$U(p, \omega) = \sum_{i=1}^n A(\omega, r_i) e^{j(\phi_i + \omega p r_i)}, \quad (1)$$

where $A(\omega, r_i)$ is the amplitude spectrum of a trace at distance r_i and ϕ_i is its phase spectrum. The observed spectrum is assumed to be the result of the superposition of M surface wave modes such that

$$A(\omega, r_i) e^{j\phi_i} = \sum_{k=1}^M S_k(\omega, r_i) e^{j(\phi_{0k}(\omega) - \omega p_{0k}(\omega) r_i)} \quad (2)$$

where $S_k(\omega, r_i)$ is the amplitude spectrum of the k 'th mode and the phase is separated into distance independent, $\phi_{0k}(\omega)$, and distance dependent, $\omega p_{0k}(\omega)$, components. If the modulus of $U(p, \omega)$ is plotted on a two dimensional plot as a function of p and ω , the $p-\omega$ locus corresponding to the largest values in $U(p, \omega)$ wave field is exactly the phase velocity dispersion curve of that particular mode, excluding the problems of aliasing.

A $p-\omega$ stack was performed on the set of traces on each side of the shot points. For example, the phase velocity contour plot for the area northeast of SP3 is shown in Figure 5. For all but one data set, the signals of the Rayleigh wave fundamental mode are coherent and the results indicate a negligible effect of lateral heterogeneity on the phase

velocity. In one data set however, the northeast profile of SP2, strong variation in the phase velocity is found. On this profile, traces that are beyond about 30 km from the origin (268-281, (Figure 2)) indicate lower phase velocity than the closer traces (283-297). Figure 6 is the $p-\omega$ stack using all traces northeast of SP2. This figure shows two dispersion curves. The lower velocity one corresponds to traces 268-281 and the upper to traces 283-297. These were recorded on the Abt schist rock formation located southwest of Al-Amar Idsas fault zone. Mooney et al. (1985) had difficulty in modeling the upper and lower crust and the upper mantle between SP1 and SP2 of the seismic profile. They suggested the presence of a strong lateral heterogeneity northeast of SP2, in which the velocity of the crust and upper mantle increases toward the northeast. The boundary they suggested to mark the transition intersects the surface about 25-30 km northeast of the shot point. This is consistent with the location of the phase velocity change. However, the phase velocities for this area are lower than the rest of the profile and the other sections by 0.3 km/s and will be shown from the inversion of this data, the velocity of the near surface material decreases to the northeast instead of increasing as do the crustal and upper mantle velocities.

From the $p-\omega$ analysis, we were able to determine the phase velocity of the fundamental mode for frequencies of 1-5 Hz. For frequencies greater than 5 Hz, the signal began to lose coherency and the function $U(p, \omega)$ no longer had a well defined maximum, due to the increase of the noise level and the effect of spatial aliasing at high frequencies. The phase velocity of the fundamental mode ranges between 2.9 km/s at 5 Hz to 3.2 km/s at 1 Hz. The maximum values on the contour plot of Figure 5 define the phase velocity dispersion curve on the northeastern side of SP3 and is plotted as curve RPF in Figure 7.

Group velocity and anelastic attenuation determination

The multiple filter technique of Dziewonski et al. (1969) was used to determine the group velocity of the different modes. Each trace was Fourier transformed and narrow

band pass filtered in the frequency domain using a Gaussian filter (Herrmann, 1973). Relative maximum spectral amplitudes and their group velocities were determined for each filter center frequency. The modal amplitudes from all the traces on one side of a shot point for each frequency window were plotted as a function of distance. Linear regression analysis was performed on the points to determine the mean and standard deviation of the group velocity. We were able to isolate the fundamental and the first higher mode by this procedure. Modes higher than these were difficult to isolate. In addition, the spectral amplitudes of the fundamental mode for each frequency window were multiplied by square root of the distance to correct for geometrical spreading. The decay of the corrected amplitude spectrum with distance was then used to estimate the Rayleigh wave anelastic attenuation coefficient γ_R using linear regression analysis according to the model

$$\ln A(r, \omega) = \ln A_0 - \gamma_R(\omega)r$$

The results indicate that the group velocity of the fundamental mode ranges between 2.5 km/s at 5 Hz and above to 3 km/s at 1 Hz. An example of the group velocity dispersion curve of the fundamental mode for the region northeast of SP3 is shown in Figure 7 (RGF). The first higher mode has a group velocity of about 3.4 km/s at 5 Hz, which decreases to 3.1 km/s at about 20 Hz (RGH1 in Figure 7). Due to the presence of lateral variations northeast of SP2, the group velocities for the distant set of traces of this shot point were determined by using the interstation arrival times of the various frequency components at the nearest and the farthest stations of this subset (two station technique). The group velocities in this section of the profile are about 0.3 km/s lower than the other profiles.

The decay of surface wave amplitude with distance is often difficult to measure due to a number of factors such as local site effects, scattering and lateral lithological changes. Despite this difficulty, it was important to try to obtain amplitude attenuation data so the anelastic properties of the earth can be determined. Meaningful measure-

ments of amplitude decay require accurate amplitude data at closely spaced stations over a considerable distance range. It is not practical to measure the decay along each geological unit to determine individual γ_R 's because of the relatively short spatial horizontal distances of these units. Thus, lateral homogeneity in anelasticity was assumed. An example of the variation of γ_R as a function of period is shown in Figure 8 for the profile SP3 northeast. Its behavior is similar to those determined from long period surface wave across continental and oceanic paths (Mitchell et al., 1977), being larger at higher frequencies. Generally, in all the profiles analyzed, γ_R decreases monotonically from 0.3 km^{-1} at 0.1 s to 0.1 km^{-1} at 0.2 s. The values of γ_R slowly decrease for periods higher than 0.2 s and reach 0.006-0.015 km^{-1} at 0.8 s periods. Strong amplitude variations due to site effect are very noticeable especially in the sections SP2 northeast and SP3 northeast. Because all the traces were used on each section, the effect of these variations on the measured γ_R was minimized.

INVERSION FOR SHEAR VELOCITY AND Q_β

The observed dispersion data combined with an initial model were used to invert for the shear velocity structure. Because of the non-linear nature of the problem, an iterative linear inversion was performed in which the model was updated after each iteration. The general linear inverse problem is governed by the equation

$$y = Ax, \quad (3)$$

where y is the difference between observed data and those predicted by the model used, and x represents the model parameter changes which are to be determined and added to the starting model after each iteration in order to minimize y . A is the matrix of partial derivatives of phase and group velocity. Russell (1980) concluded that the first order difference technique provides the best constraint on the inversion of surface wave data, especially in the presence of noisy data. This differential damped least square inversion controls the smoothness of the resulting models by seeking to minimize the differences in the interlayer model changes (Twomey, 1977). This type of constraint was used in this

study, and the inversion of shear velocity was performed using a starting model that consisted of very thin layers (50-100 m) with the same model parameters at all depths, for an inversion unbiased by the initial model. We started with a P-wave velocity (α) of 7 km/s and a Poisson ratio of 0.25 for the initial model (S-wave velocity, $\beta=4.04$ km/s) in each layer. During the inversion, Poisson's ratio was fixed and the shear velocities allowed to vary.

Inversion of the observed γ_R values to determine Q_β was performed following Mitchell's (1975) formulation of the problem, where the spatial attenuation coefficient is written as

$$\gamma_R = \frac{\pi}{T} \left[\sum_{i=1}^n \frac{\partial c_R}{\partial \alpha_i} \frac{\alpha_i}{c_R^2} Q_{\alpha_i}^{-1} + \sum_{i=1}^n \frac{\partial c_R}{\partial \beta_i} \frac{\beta_i}{c_R^2} Q_{\beta_i}^{-1} \right]. \quad (4)$$

In (4), n is the total number of layers, c_R is the phase velocity of Rayleigh waves, α and β are the compressional and shear velocities of the layer i , and T is the period. Assuming no bulk losses, Q_α is related to Q_β by (Anderson et al., 1965)

$$Q_\beta^{-1} = \frac{4}{3} \left(\frac{\beta}{\alpha} \right)^2 Q_\alpha^{-1}. \quad (5)$$

This equation was used to simplify (4) which was then put in the form of (3) for the purpose of inversion. The partial derivatives of the phase velocity were determined for the inverted shear velocity model for the profile. Singular value decomposition of A for both the shear velocity and Q_β^{-1} was performed as described by Lawson and Hanson (1974).

The inverted shear velocity and Q_β models are shown in Figures 7 and 8, respectively, for the SP3NE data set and in Figure 9 for all the profiles. In general, the velocity structure consists of two regions: a surface layer 0.3-0.4 km thick in which the shear wave velocity increases rapidly from 2.6 km/s to 3.3 km/s, overlying a half space with shear wave velocity of 3.4-3.5 km/s. The resolution decreases with depth and the velocity for the layers deeper than 1.0 km is considered unresolved. The use of the higher mode group velocity data in the velocity inversion resulted in better resolution and a

stable model for depths greater than 400 m.

The velocity structures along the profiles SP2 northeast and SP2 southwest showed the most complexity and variation. The group and phase velocities are higher to the northeast of the shot point (283-297) than to in the southwest, and in both cases a region of low velocity was required by the inversion. In the southwest, β increases from 2.8 km/s near the surface to 3.4 km/s at 0.3 km depth and then decreases to 3.25 at 0.5 km depth. The velocity increases again in the deeper layers. To the northeast (Figure 9, SP2NE(a)), the velocity increases from 2.7 km/s near the surface to 3.5 km/s at 0.25 km depth. It decreases to reach 3.35 km/s at 0.45 km depth and then it increases again to reach 3.6 km/s at about 0.75 km depth. Further to the northeast (Figure 9, SP2NE(b)) a low shear velocity of 2.8 km/s extends to 0.25 km depth. The velocity increases below this depth to reach 3.2 km/s at 0.5 km. These results indicate that the granite gneiss located northeast of the shot point has a higher seismic velocity in the Shammar province than the Abt schist.

The results of the Q_{β}^{-1} inversion are also shown in Figure 9. A decrease in Q_{β}^{-1} with depth is coincident with the increase in β . Q_{β} increases from 30-50 near the surface to 150 at a depth of about 0.5 km, below which the inverted models are not very well resolved. The Q_{β}^{-1} models indicated by the dashed lines represent the modifications required to the models in order to match synthetic seismograms to observed data.

Attenuation in the northeastern section of SP4 is higher than to the southwest, as indicated by the inversion. Q_{β}^{-1} decreases from 0.018 near the surface to 0.007 at 0.5 km depth. To the northeast, Q_{β}^{-1} decreases slowly from 0.02 near the surface to 0.014 at 0.5 km. However, the attenuation model for the northeast profile required by the synthetic modeling is similar to that of the southwestern section. Similar models found from the inversion of γ_R on both sides of SP3 show a decrease of Q_{β}^{-1} from about 0.025 near the surface, to 0.004 at 0.5 km depth in the northeast and from 0.025 to 0.0075 in the southwest. The results of the Q_{β}^{-1} inversion for SP2 indicate higher attenuation than

other shot points, coinciding with the lower shear velocity. Q_{β}^{-1} decreases from 0.027 near the surface to 0.016 at 0.5 km depth for the distant traces northeast of SP2 (Figure 9, SP2NE(b)).

WAVEFORM MODELING

To verify the correctness of the inverted models and to understand the poorly resolved deeper Q_{β}^{-1} , surface-wave synthetic seismograms of both the fundamental and the first higher modes were calculated using the computer programs developed by Wang (1981). The computations are made stable at high frequencies for relatively complex models by the introduction of compound matrices in the Haskell-Thompson propagator matrix technique. Wang and Herrmann (1980), Herrmann and Wang (1985), and Wang (1981) give explicit formulas for ten Green functions to describe the wave field due to an arbitrary point dislocation source and a point explosion. The calculations performed in this study are for the vertical component of motion due to a center of compression seismic source.

With the velocity and Q structure determined by inversion, we need only to specify the time history of the explosion sources in order to compute the synthetic seismograms. We tried both a step and a Dirac delta source time functions for the three orthogonal force dipoles of the source. It is commonly assumed that a step is an adequate representation of the source time function for long period surface waves from explosions (Tsai and Aki, 1970). O'Brien (1967) uses an exponential step to describe the source spectrum of small charges. The analysis of our study indicates that a step source time function does not generate enough of the high frequency components observed on the seismograms. Although the exact source spectrum is not known, we prefer a Dirac delta function to represent the source time function at this distance range. In addition to producing the proper frequency content of the signal, the use of this type of source time function results in a better fit to the onset of the observed signal.

Both the recorded data and the computed synthetics are the output voltage of the geophone, being proportional to ground velocity at frequencies greater than the natural frequency of 2 Hz. The instrument response was included in the synthetics by using a recursive digital filter, and the source depth is fixed at 60 m for all shot points. Theoretical phase velocities calculated from the inverted seismic models were corrected for the dispersion due to anelasticity using the correction factor given by Liu et al. (1976). Since we are interested in the decay of amplitude with distance rather than the absolute amplitude, all synthetics were generated using a constant source size

Examples of the results of the waveform modeling are shown in Figure 10. Each observed and synthetic trace was filtered using a bandpass Butterworth filter with corner frequencies 1 and 10 Hz. The amplitudes were normalized and a 9 second reduced travel time window that contains both the fundamental and the higher mode signal was plotted. The Q_{β}^{-1} of the very upper most layers were adjusted to obtain a better fit between the observed and the synthetic fundamental mode waveforms by trial and error (as shown by the dashed line in Figure 9). This is justified by the lack of resolution in the inversion for Q_{β}^{-1} in these layers. However, the velocity models were used without any change. Q_{β} of the layers beneath 500 m could not be resolved in the same way since it does not affect the fundamental mode wave dispersion. An estimate of the attenuation of the deeper layers is obtained by using the ratio of the maximum spectral amplitude of the fundamental to that of the first higher mode. The site effects were canceled out by taking the ratio of two signals from the same trace. The synthetic seismograms were first computed on the basis of the models obtained from inversion. Q_{β}^{-1} at depth was then adjusted to obtain agreement between the change with distance of the higher mode amplitude relative to the fundamental mode amplitude. The fundamental and higher mode signals were isolated in the time domain and the spectral amplitude of each was determined. A search was performed to determine the maximum spectrum of each signal, and the ratio of the maximum spectral amplitude of the fundamental to that of the

higher mode was compared with that of the synthetic for estimation of Q_{β}^{-1} at depth, as shown in Figure 11.

Figure 10b shows that the fundamental mode arrival times and waveforms are successfully modeled for the section SP3 northeast using $Q_{\beta}=30$ for the first 100 m, which increases gradually below this depth to reach about 150 at a 400 m depth (Figure 9). We were not able to reproduce the observed higher mode amplitudes using a step source time function even for very high Q values ($Q_{\beta}\approx 2000$), as shown in Figure 10c. Reasonable correlation was obtained from a delta source using a Q_{β} of 500 at depth (Figure 10b). The wide scatter in the amplitude ratio of the spectral maximum of the fundamental and the higher mode is shown in Figure 11. This might be due to complexity in the vertical distribution of Q due to structural or lithologic variations that is not revealed by the surface geology. The ratio oscillates between 3 and 8 where the profile traverses the granite and drops to 3-4 in the Halaban formation. For the profile SP3 southwest, the waveform modeling requires a Q_{β} model that increases from 30 in the first 50 m to 110 at 400 m depth. Below this depth the average Q_{β} of the Halaban formation southwest of SP3 is about 400.

Similar results were also obtained for the profiles of SP4 northeast and southwest. Although the signal to noise ratio is low compared to that of the sections from SP3, the various components of the fundamental mode can be correlated with the synthetics throughout the length of the profiles. Q_{β} in profile 4 northeast is 30 near the surface and increases slightly to 50 at 100 m depth, continues unchanged to 300 m. An increase in the high frequency content of the signals is observed at distances beyond about 35 km northeast of SP4 where the stations are located on alternating units of granite and green-schist. It is clearly evident in Figure 11 that we could not fit the observed data for the close and distant stations by one Q model. The synthetics of SP4NE were obtained using Q_{β} of 500 below 400 m. At distances short to the shot point where the Hali schist and the granite outcrops, this value is higher than the apparent shear quality factor. Where

the greenschist outcrops at greater distances, Q_β is probably higher than 500. Thus, the Hali schist and the adjacent granite of the Hijaz-Asir tectonic province have lower Q_β than the greenschist. This conclusion is more obvious for the section to the southwest where Q_β of about 700 is used to produce the synthetic traces southwest of SP4. Again, the attenuation in the formations at close distance is higher than the distant formation, where the stations are located on greenschist rock, as is evident by the drop of the ratio in Figure 11. Q_β increases from 28-30 near the surface to about 150 at 500 m depth for this profile.

Waveform models of the seismic traces from southwest of SP2 were also computed. The one dimensional velocity model and the Q_β model in Figure 9 were used to produce the synthetic seismograms. A good fit was obtained using Q_β that increases from 30 in the first layer to 150 at a depth of 600 m. The synthetic ratio of the maximum spectral amplitude could not be correlated with the observed one using a low attenuation zone at depth. Although large scatter exists at short distances in Figure 11, a ratio of about 2 is maintained at distances greater than 35 km. The observed higher mode signal is strongly attenuated at short distances where the stations are located on the Halaban and the Murdama formations, and as soon as the granite and the granite gneiss are crossed, the higher mode amplitude and in general the high frequency content of the traces are increased. The Q_β for the granite and the granite gneiss is higher than 500, and the observed ratio can be fit using Q_β of 700. Due to the strong lateral heterogeneity in the velocity northeast of SP2, no synthetic seismograms were calculated for this section.

CONCLUSION

A straightforward method for determining seismic structure of the upper few hundred meters using high frequency surface waves has been presented in this study. The data used are short period Rayleigh waves obtained from recorded deep seismic refraction profiles across the shield at distances of up to 55-80 km from the shot points.

The shear wave velocity increases from 2.6 km/s near the surface to 3.4 km/s at about 0.4 km depth. The average Q_β for the Arabian shield is found to be very low near the surface, increasing from 30 near the surface to 150 at a depth of about 0.5 km. The Q_β for the crust between 0.5 and 1.0 km depth ranges from 400-700 and is probably higher. Metamorphic rocks that are characterized by lineation, such as schist, have a lower Q_β than igneous rocks, such as granite.

The uniform distribution of the velocity structure of the upper crust of the shield found from the P-wave travel time data (Mooney et al., 1985) also characterizes the S-wave structure in the upper one kilometer of the shield. The major crustal inhomogeneity at the northeast end of the profile (northeast of SP2) is also reflected in the subsurface material in the region covered by the Abt schist. This rock formation may contain unidentified thrust faults as suggested by Delfour (1979), which may explain its low seismic velocity and Q values. The presence of faulting and lineations in the rock may lower their shear wave velocities and Q_β .

Gettings and Showail (1982) measured the heat flow at several drill holes of the shot points in the refraction line. The results of their measurements indicate that the heat flow increases toward the Red Sea margin. The heat flow at SP2 is probably lower than that in SP3 and SP4, but large uncertainties of the data does not permit any definite conclusions. We can not establish any relation between heat flow and the distribution of the shallow Q at these three shot points. In fact, the attenuation is lower southwest of SP4 where the heat flow is presumed to be relatively higher. Despite the geological complexity of the region, these results show that high frequency surface waves can provide information about the upper crust that would be difficult to determine using other methods.

The techniques presented here will also work with ground roll signals observed in exploration data sets. Ground roll signals can be used to study the lateral variation of shallow shear-wave velocities and attenuation in the weathering layers which can be

useful in constraining shear-wave statics, and more importantly, in understanding the nature of the ground roll signal so that data acquisition and processing can be designed to remove it from the desired exploration signal.

ACKNOWLEDGMENTS

We would like to thank Habib Merghalani of the Directorate General of Mineral Resources of the Ministry of Petroleum and Mineral Resources of the Kingdom of Saudi Arabia as well as Walter Mooney of the United States Geological Survey for providing a magnetic tape of the recorded seismic refraction data.

REFERENCES

- Al-Husseini, M. I., Glover, J. B., and Barley, J., 1981, Dispersion patterns of the ground roll in eastern Saudi Arabia: *Geophysics*, **46**, 121-137.
- Anderson, D. L., Ben-Menahem A., and Archambeau C. B., 1965, Attenuation of seismic energy in the upper mantle: *J. Geophys. Res.*, **70**, 1441-1448.
- Brown, G. F., and Jackson, R. O., 1979, An overview of the geology of western Arabia: U.S. Geol. Surv. Saudi Arabian project report **250**.
- Delfour, J., 1979, Geologic map of the Halaban quadrangle sheet 23G, Kingdom of Saudi Arabia: Saudi Arabia Directorate General of Mineral Resources, geologic map, GM-46A, scale 1:250,000.
- Dziewonski, A. M., Bloch S., and Landisman M., 1969, A technique for the analysis of transient seismic signals: *Bull., Seis. Soc. Am.*, **59**, 427-444.
- Gettings, M. E., and Showail A., 1982, Heat flow measurements at shot points along the 1978 Saudi Arabian deep-seismic refraction line, I, Results of the measurements: U.S. Geol. Surv. open-file rep. 2-39.
- Greenwood, W. R., Anderson, R. E., Fleck, R. J., and Roberts, R. J., 1980, Precambrian geologic history and plate tectonic evolution of the Arabian Shield: Saudi Arabian Directorate General of Mineral Resources Bull. **24**.
- Healy, J. H., Mooney, W. D., Blank H. R., Gettings, M. E., Kohler, W. M., Lamson, R. J.,

- and Leone, L., 1982, Saudi Arabian seismic deep-refraction profile, final project report: U.S. Geol. Surv. Saudi Arabian Mission open-file rep. 2-37.
- Herrmann, R. B., 1973, Some aspects of band-pass filtering of surface waves, *Bull., Seis. Soc. Am.*, **63**, 663-671.
- Herrmann, R. B., and Wang, C. Y., 1985, A comparison of synthetic seismograms: *Bull., Seis. Soc. Am.*, **75**, 41-56.
- Knopoff, L., 1972, Observation and inversion of surface wave dispersion: *Tectonophysics*, **13**, 497-519
- Knopoff, L., and Fouda, A. A., 1975, Upper mantle structure under the Arabian Peninsula: *Tectonophysics*, **26**, 121-134
- Kovach, R. L., 1978, Seismic surface waves and crustal and upper mantle structure: *Rev. Geophys. Space Phys.*, **16**, 1-13
- Lawson, C. L., and Hanson, R. J., 1974, *Solving least squares problems*: Prentice-Hall, Inc.
- Liu, H. P., Anderson, D. L., and Kanamori, H., 1976, Velocity dispersion due to anelasticity; implications for seismology and mantle composition: *Geophys. J. Roy. Astr. Soc.*, **47**, 41-58.
- McMechan, G. A., and Yedlin, M. J., 1981, Analysis of dispersive waves by wave field transformation: *Geophysics*, **46**, 869-874.
- Mitchell, B. J., 1975, Regional Rayleigh wave attenuation in North America: *J. Geophys. Res.*, **80**, 4904-4916.
- Mitchell, B. J., Yacoub, N., K., and Correig, A. M., 1977, A summary of surface wave attenuation and its regional variation across continents and oceans, in Heacock, J. G., Keller, G. V., Oliver, J. E., and Simmons, G., Eds., *The Earth's crust*: Am. Geophys. Union, *Geophys. Mono.* **20**, 405-425.
- Mooney, W. D., Gettings M. E., Blank H. R., and Healy J. H., 1985, Saudi Arabian seismic-refraction profile: A travel time interpretation of crustal and upper mantle

- structure: *Tectonophysics* , **111** , 173-246.
- Niazi, M., 1968, Crustal thickness in the Saudi Arabian Peninsula: *Geophys. J. Roy. Astr. Soc.*, **15** , 545-547.
- O'Brien, P. N. S., 1967, The efficient use of large charges (on dispersed land shots, underwater explosions, and atmospheric explosions), in Musgrave, A. W., Ed., *Seismic refraction prospecting: Soc. Expl. Geophys.*, 152-170.
- Russell, D. R., 1980, Constrained inversion techniques applied to surface wave analysis: M.Sc. Thesis, Univ. of Texas El Paso.
- Schmidt, D. L., Hadley D. G., and Stoesser D. B., 1978, Late Proterozoic crustal history of the Arabian shield, Southern Najd province, Kingdom of Saudi Arabia: *U.S. Geol. Surv. Saudi Arabian Mission rep.* 251.
- Tsai, Y. B., and Aki, K., 1970, Precise focal depth determination from amplitude spectra of surface waves: *J. Geophys. Res.*, **75** , 5729-5743.
- Twomey, S., 1977, Introduction to the mathematics of inversion in remote sensing and indirect measurements: Elsevier Science Publ. Co., Inc.
- Wang, C. Y., 1981, Wave theory for seismogram synthesis: Ph.D. Dissertation, Saint Louis University.
- Wang, C. Y., and Herrmann, R. B., 1980, A numerical study of P-, SV-, and SH- wave generation in a plane layered medium: *Bull., Seis. Soc. Am.*, **70** , 1015-1036.

LIST OF FIGURES

FIG.1. Index maps of the study region showing (a) the location of the seismic deep refraction profile (heavy line) with tectonic provinces and (b) a geologic cross section across the Arabian shield. The extent of the profiles used in this study are shown by heavy lines in (b). The lithologic units of the geologic cross section are as follow: a - Abt schist, b - greenstone, c - clastic rocks, d - granodiorite and diorite, g - calc-alkaline granite, gr - granite, h - andesite, m - Murdama formation, n - granite gneiss, r - peralkaline granite, s - greenschist, w - Hali schist. F indicates faulting.

FIG.2. The recorded seismic traces from SP2 plotted in reduced travel time (reproduced from Healy et al., 1982). Positive and negative distances are to the northeast and the southwest of the shot point, respectively.

FIG.3. The recorded seismic traces from SP3 (reproduced from Healy et al., 1982). Positive and negative distances are to the northeast and the southwest of the shot point, respectively.

FIG.4. The recorded seismic traces from SP4 (reproduced from Healy et al., 1982). Positive and negative distances are to the northeast and the southwest of the shot point, respectively.

FIG.5. Dispersion contour plot showing the modulus of $U(p, \omega)$ from the SP3 northeast profile as a function of frequency and phase velocity (see text). The maximum values of the contour plot define the dispersion curve. The contours are at 0.9, 0.8, 0.7, 0.6, 0.5 of the maximum of $U(p, \omega)$ at a given frequency.

FIG.6. Dispersion contour plot for the SP2 northeast profile. The plot suggests two distinct dispersion relations. The higher phase velocities are associated with the set

of traces at distances < 31 km (283-297). The lower phase velocities are associated with the traces at distances > 31 km (268-281).

FIG.7. Observed Rayleigh wave dispersion curves (x's) and theoretical curves (lines) obtained from the shear velocity model at the left for the section SP3 northeast. RPF is the phase velocity of the fundamental mode, RGF is the group velocity of the fundamental mode, and RGH1 is the first higher mode group velocity.

FIG.8. Observed (circle) and theoretical (line) spatial attenuation coefficient of the fundamental mode Rayleigh waves as a function of period for the profile SP3 northeast. The inset is the Q_β model inverted from the observed data.

FIG.9. The results of shear wave velocity and Q_β^{-1} inversions for the different profiles used as indicated at the top of the figure. For the section SP2 northeast, (a) is for the region occupied by stations 283-297, and (b) is for the region occupied by stations 268-281. The dashed lines in the Q_β^{-1} models show the adjustments made in the inverted models to successfully match observed seismograms with synthetics.

FIG.10. Waveform modeling results for the profile SP3 northeast. The plots represent 9 second windows of the reduced travel time. (a) is the observed data bandpass filtered between 1.0 and 10.0 Hz. (b) and (c) are obtained using delta and step source time functions, respectively.

FIG.11. The ratio of the maximum spectral amplitude of the fundamental to that of the first higher mode plotted as a function of distance from the source. The asterisks are derived from synthetics using the dashed Q^{-1} models in Figure 9.

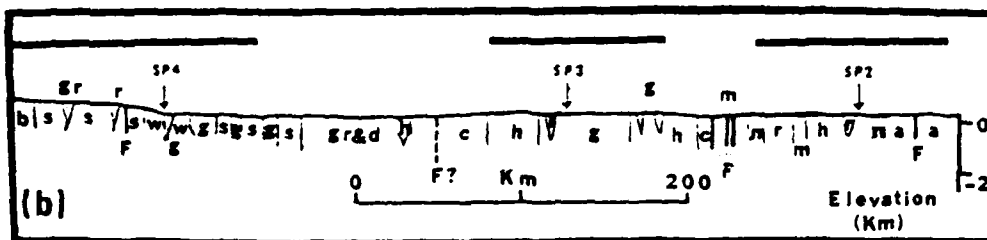
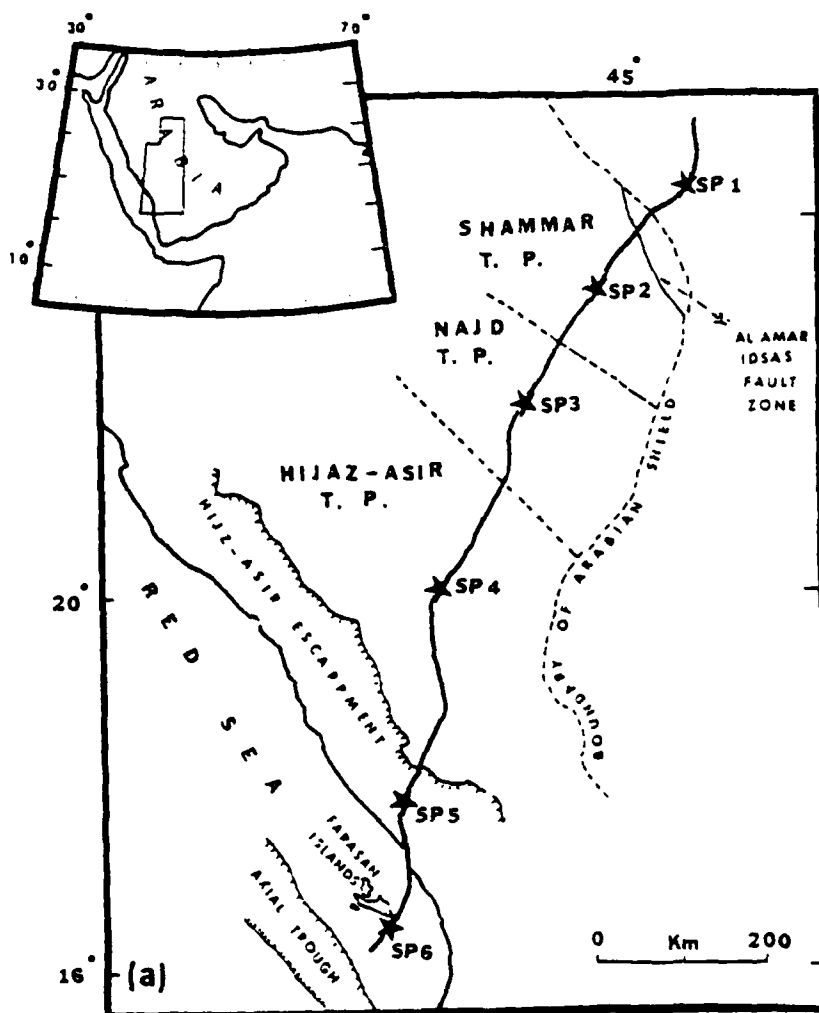


FIG.1. Index maps of the study region showing (a) the location of the seismic deep refraction profile (heavy line) with tectonic provinces and (b) a geologic cross section across the Arabian shield. The extent of the profiles used in this study are shown by heavy lines in (b). The lithologic units of the geologic cross section are as follow: a - Abt schist, b - greenstone, c - clastic rocks, d - granodiorite and diorite, g - calc-alkaline granite, gr - granite, h - andesite, m - Murdama formation, n - granite gneiss, r - peralkaline granite, s - greenschist, w - Hali schist. F indicates faulting.

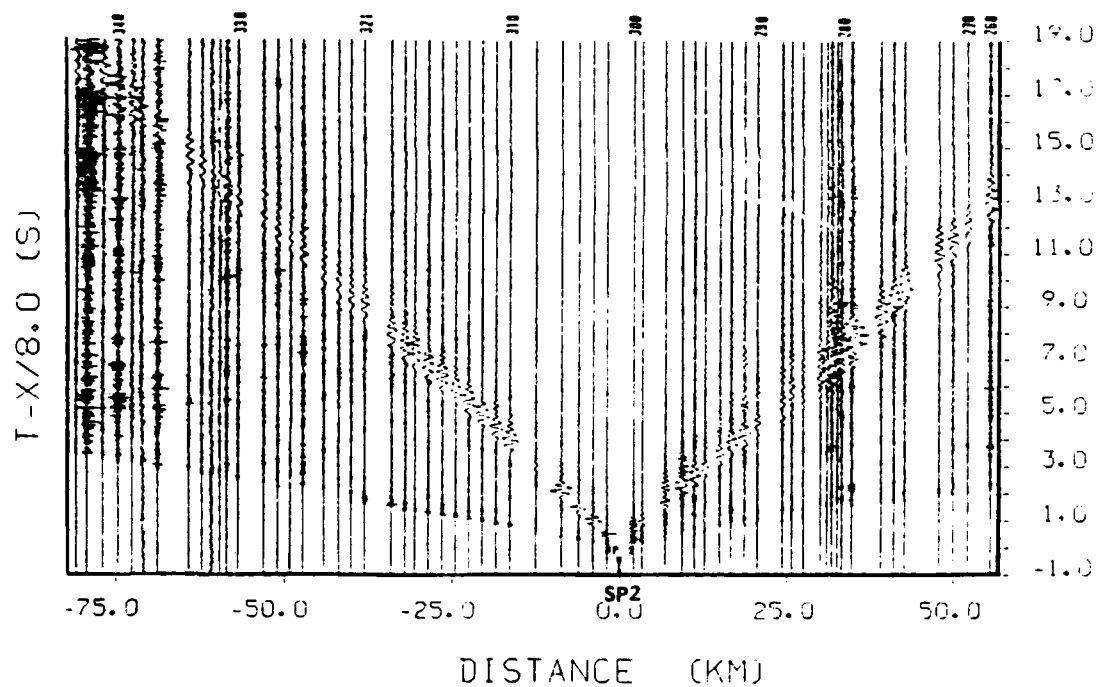


FIG.2. The recorded seismic traces from SP2 plotted in reduced travel time (reproduced from Healy et al., 1982). Positive and negative distances are to the northeast and the southwest of the shot point, respectively.

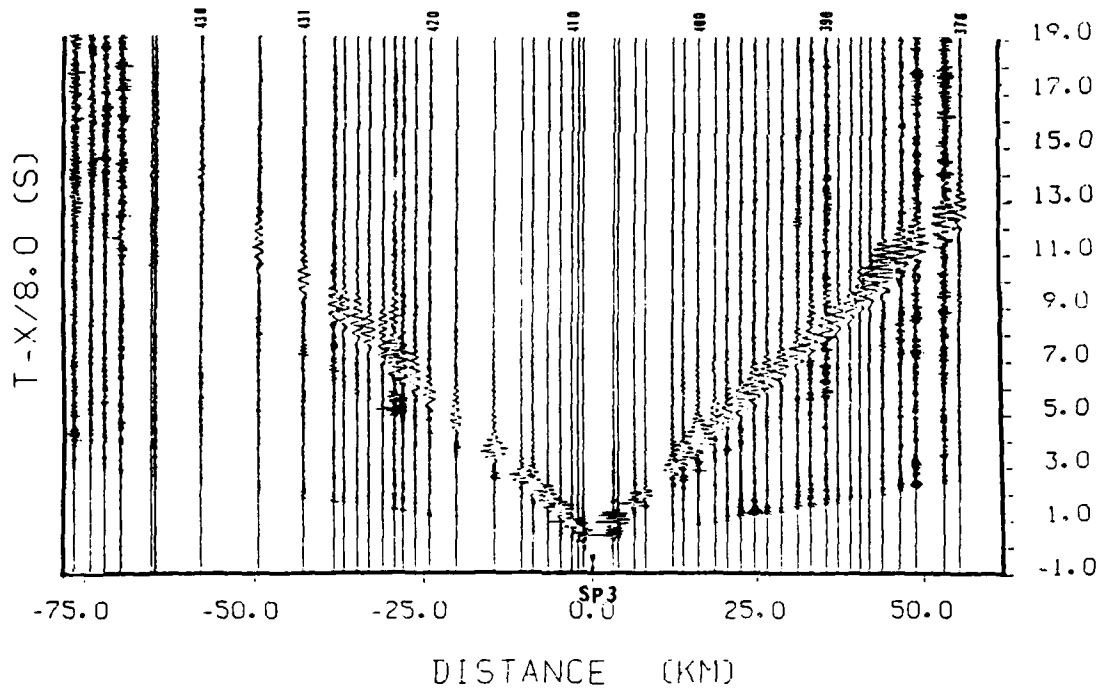


FIG.3. The recorded seismic traces from SP3 (reproduced from Healy et al., 1982). Positive and negative distances are to the northeast and the southwest of the shot point, respectively.

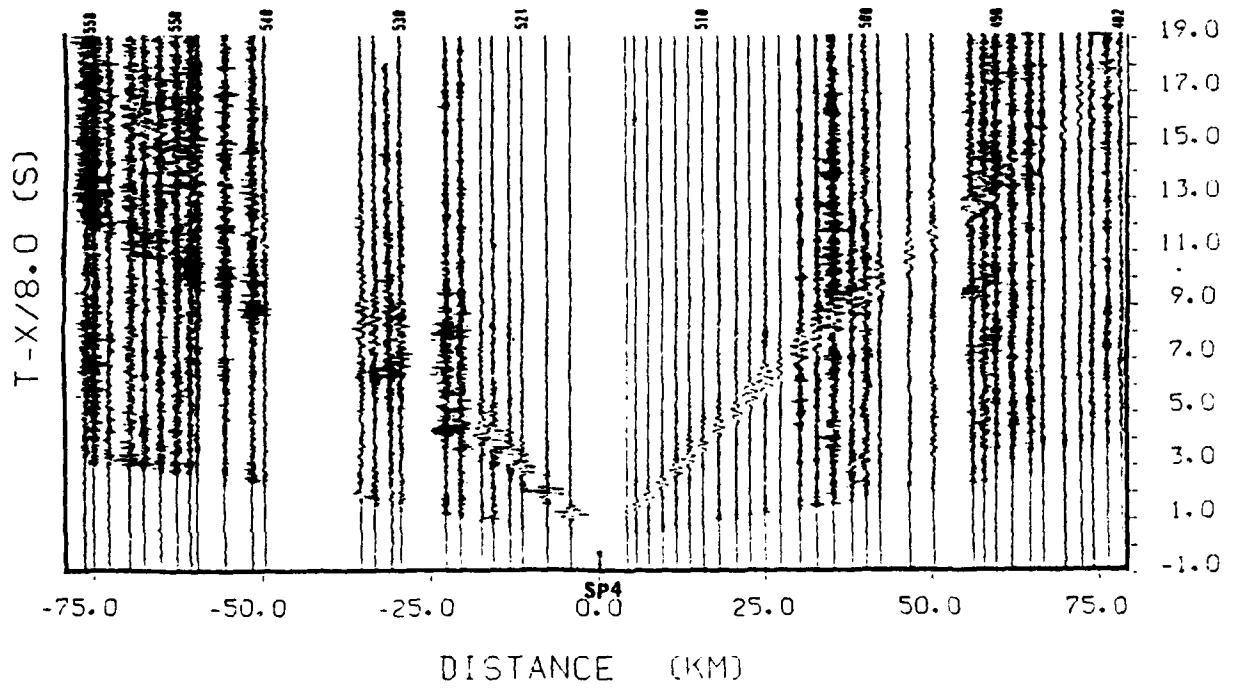


FIG.4. The recorded seismic traces from SP4 (reproduced from Healy et al., 1982). Positive and negative distances are to the northeast and the southwest of the shot point, respectively.

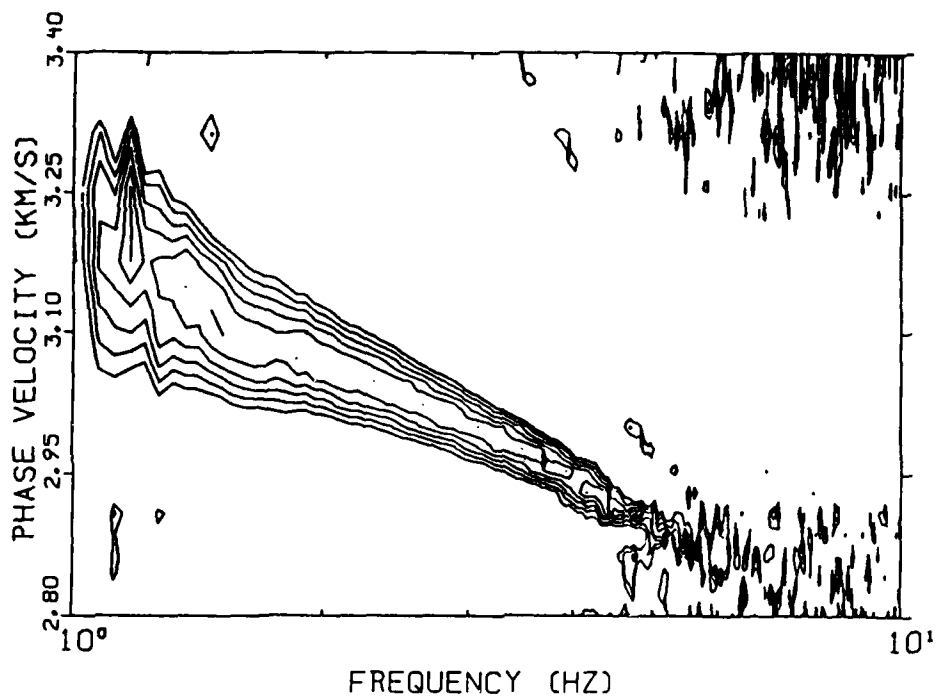


FIG.5. Dispersion contour plot showing the modulus of $U(p, \omega)$ from the SP3 northeast profile as a function of frequency and phase velocity (see text). The maximum values of the contour plot define the dispersion curve. The contours are at 0.9, 0.8, 0.7, 0.6, 0.5 of the maximum of $U(p, \omega)$ at a given frequency.

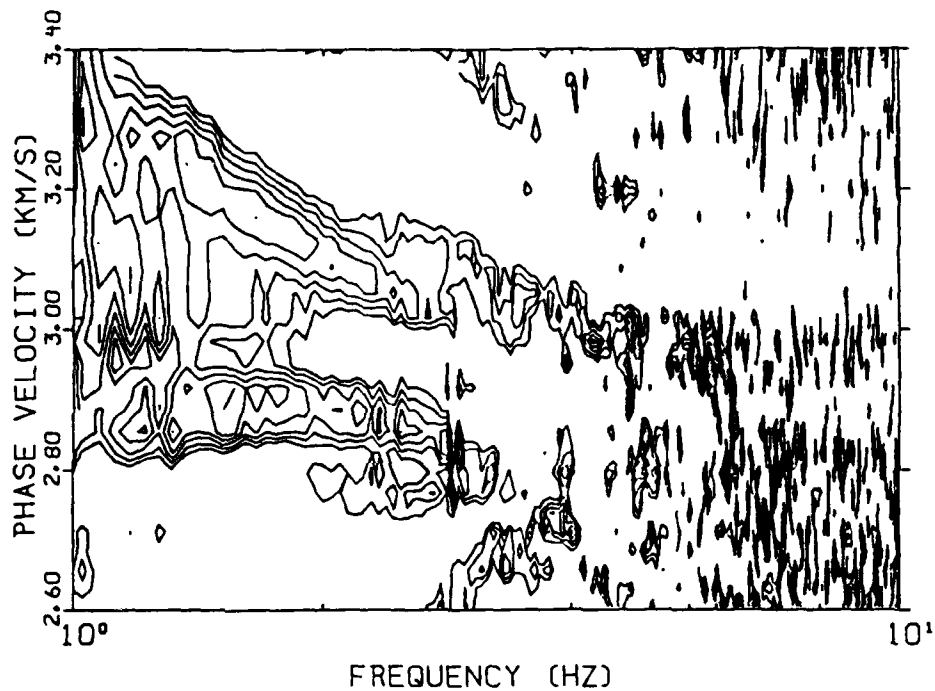


FIG.6. Dispersion contour plot for the SP2 northeast profile. The plot suggests two distinct dispersion relations. The higher phase velocities are associated with the set of traces at distances < 31 km (283-297). The lower phase velocities are associated with the traces at distances > 31 km (268-281).

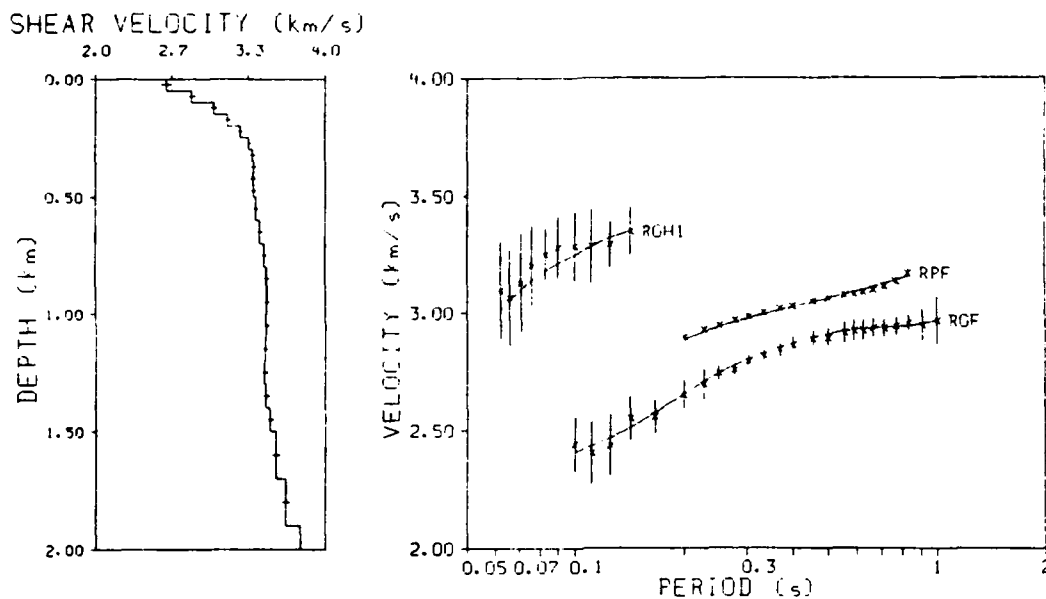


FIG.7. Observed Rayleigh wave dispersion curves (x's) and theoretical curves (lines) obtained from the shear velocity model at the left for the section SP3 northeast. RPF is the phase velocity of the fundamental mode, RGF is the group velocity of the fundamental mode, and RGH1 is the first higher mode group velocity.

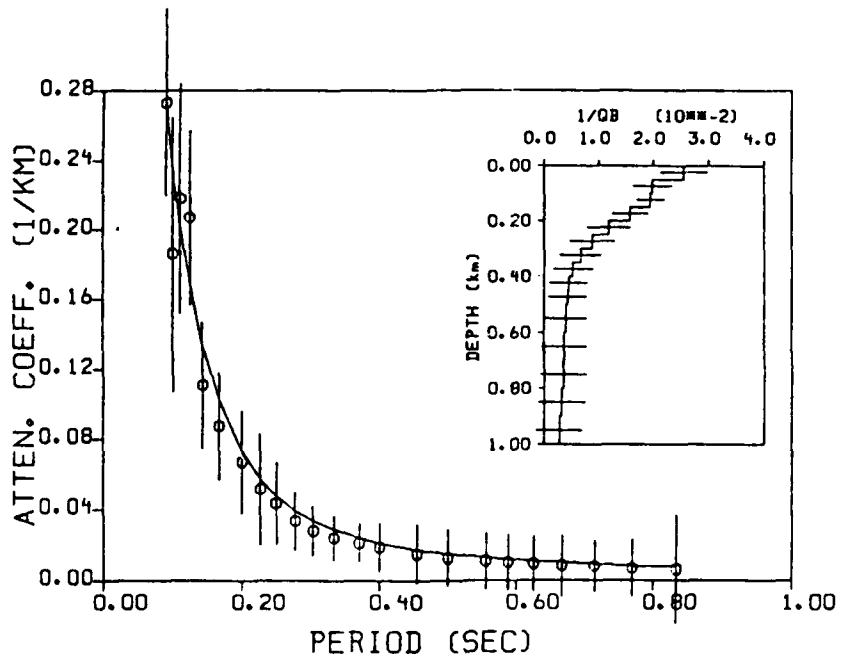


FIG.8. Observed (circle) and theoretical (line) spatial attenuation coefficient of the fundamental mode Rayleigh waves as a function of period for the profile SP3 northeast. The inset is the Q_β model inverted from the observed data.

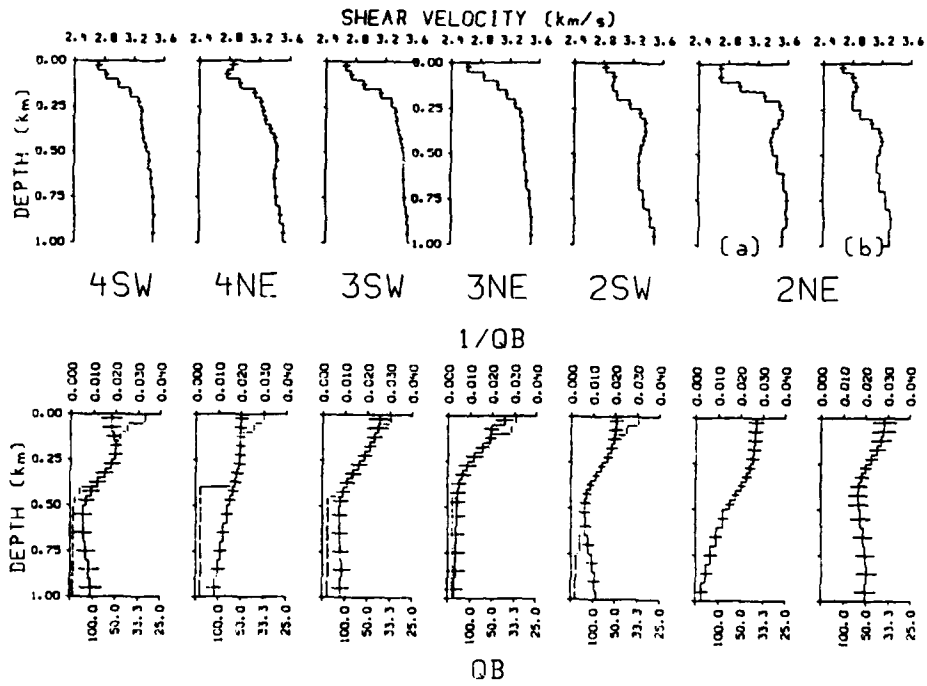


FIG.9. The results of shear wave velocity and Q_B^{-1} inversions for the different profiles used as indicated at the top of the figure. For the section SP2 northeast, (a) is for the region occupied by stations 283-297, and (b) is for the region occupied by stations 268-281. The dashed lines in the Q_B^{-1} models show the adjustments made in the inverted models to successfully match observed seismograms with synthetics.

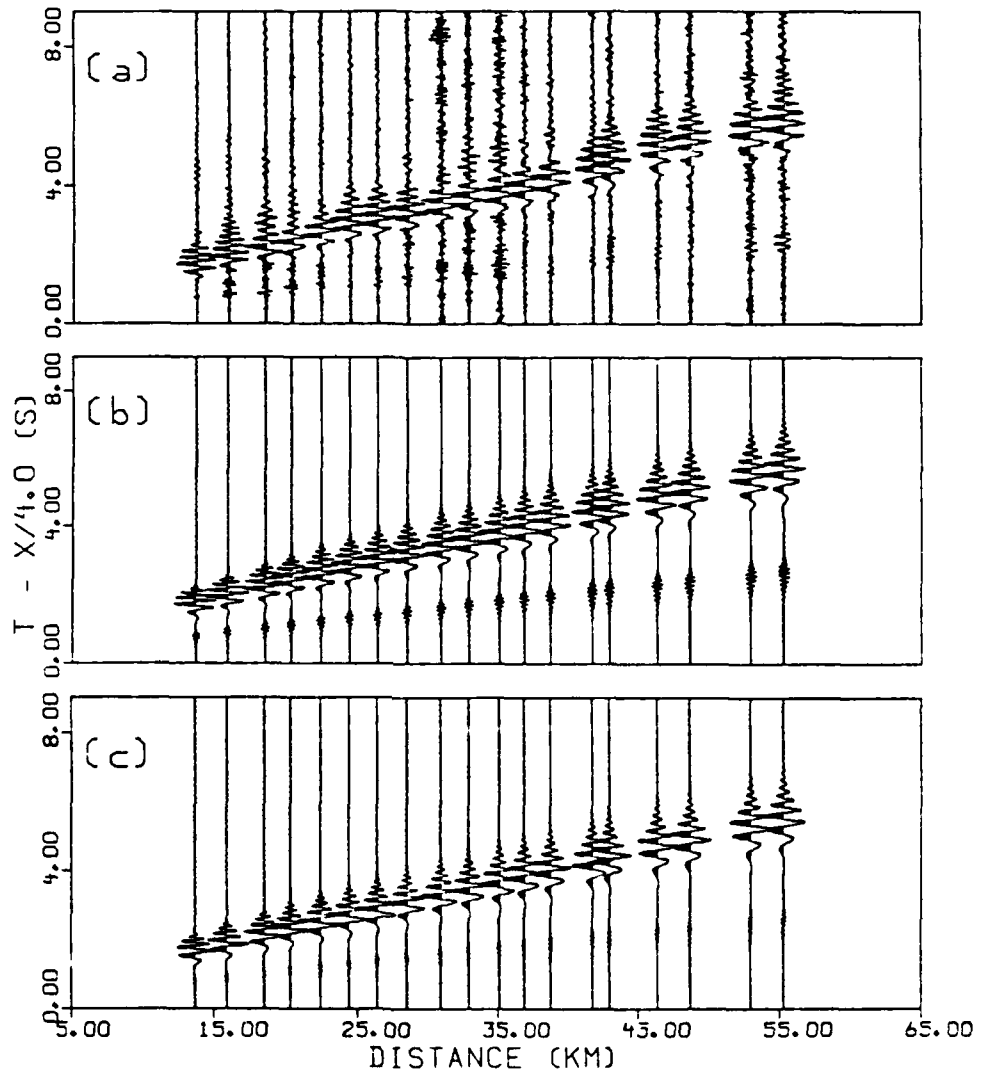


FIG.10. Waveform modeling results for the profile SP3 northeast. The plots represent 9 second windows of the reduced travel time. (a) is the observed data bandpass filtered between 1.0 and 10.0 Hz. (b) and (c) are obtained using delta and step source time functions, respectively.

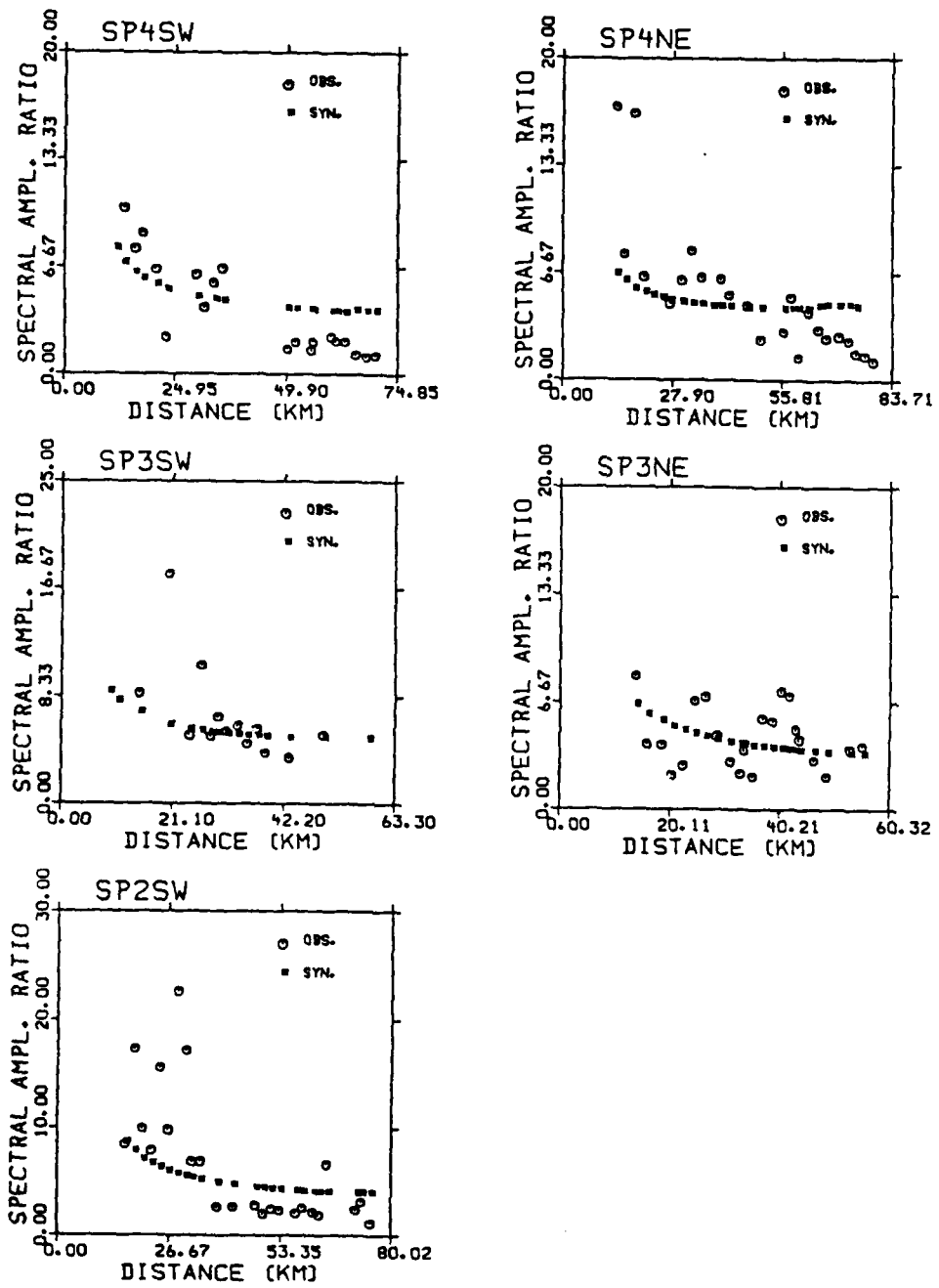


FIG.11. The ratio of the maximum spectral amplitude of the fundamental to that of the first higher mode plotted as a function of distance from the source. The asterisks are derived from synthetics using the dashed Q^{-1} models in Figure 9.

COMPUTER PROGRAMS IN SEISMOLOGY

INTRODUCTION

Following the installation of a PDP 11/70 minicomputer in 1979 for use in seismic network analysis, a persistent effort has been made to use this tool for research. Because of an obligation felt for use of the PDP 11/70 as well as a desire to do something for the world wide seismological community, a set of computer programs emerged. The programs actually developed reflect research interests of the department as well as a desire to look at data in the manner of other investigators. In doing so, the hope is that these tools will permit research to progress rapidly.

The programs are oriented toward wave propagation in plane layered media. While not as significant as recent developments in wave propagation in heterogeneous media, these programs are useful to test these new techniques in the special case of lateral homogeneity as well as to provide Green's functions required for boundary integral solutions of wave propagation in complex media. To guard against major errors, synthetic seismograms have been computed using wavenumber integration and surface-wave superposition based on Haskell matrices and Cagniard-de Hoop techniques for a comparison using independent formulations. The formulations used and numerical techniques have been published in a series of papers for reference.

Since graphical output is essential to data analysis, a output device/computer independent graphics package is provided that provides a CALCOMP/PLOT10 graphics interface to the FORTRAN and C programmer. All programs in the VOLUMES use this package, thus guaranteeing that the VOLUMES are a unified package of programs.

The programs have been developed and run under various flavors of UNIX. All of the FORTRAN code has been compiled and tested on a RIDGE 32, MASSCOMP 545, SUN 3/260 and an HP 9000. Some parts of the package have been run on a PDP 11/70 running 2.9BSD UNIX and on a CRAY 2 running CSOS. This testing effort has hopefully led to a formulation in FORTRAN that accounts for the many variations in

FORTRAN and also for the many flavors of the FORTRAN to C interface.

Substantial effort has been placed to create a computer software platform to do the research that I would like to do. It is hoped that others will be able to quickly build upon the work done.

Binary executable images for the SUN 3 computers together with documentation are available on line at the Center for Seismic Studies. The programs maintained on line at CSS are the most up to date versions.

The contents of the volumes and a short description of the programs follow. The annotation 'PC' indicates that a binary version of the program is available to run on PC computers under MS-DOS or PC-DOS. The date annotated in the last column indicates the installation date of new modules to the program distribution. are as follow:

VOLUME I - LIBRARIES

calplot(lib)	Calplot graphic libraries	PC
calplot(cmd)	Device dependent drivers	PC
four	FFT tutorial	
stoz	Bilinear Z transform	
butt	Butterworth recursive filter tutorial	

VOLUME II - GENERAL PURPOSE/SPECTRAL ANALYSIS

edabac	Epicentral distance, back azimuth, P,S times		
exspec	spectral analysis format	PC	
julday	julian day -> date		
range	distance on a sphere		
stereo	stereographic nets		
xspedt	edit dispersion curves		
xspcrd	convert digitizer output to x,y stream		
xspint	convert x,y stream to interpolated y values	PC	
xspfft	convert equispaced y values to Fourier spectra	PC	
xspdec	decimate time series in frequency domain	PC	
xspins	apply/remove instrument response	PC	
xspmft	multiple filter analysis	PC	
xspplt	plot amplitude spectra	PC	
xspgom	get phase velocities from array data	PC	
xsprot	rotate horizontal spectra to form R, T spectra	PC	
xspspc	Shell script driver for spectral analysis		
xsptrc	plot traces from spectra	PC	
xsppro	plot record section	PC	0888
xspgom	group velocity stack	PC	0888
xspmat	batch phase match filter		0888
xsp10	convert exspec to file10 format		0888
xyztpt	convert strike,dip,slip to P,T axes		
xyplt	general plotter of (x,y) values		

VOLUME III - SURFACE WAVE

surface85	obtain dispersion curves
reigen85	Rayleigh wave eigenfunction
leigen85	Love wave eigenfunction
wig85	form G(r,f) spectra
gle85	form G(r,t) time history
spec85	display G(r,f) spectra
dpsrf85	display phase velocity dispersion
srfcomb85	de-glitch dispersion curve
dpegn85	display C,U, gamma, etc
deriv85	display derivatives or eigenfunctions

pickgn85	select eigenfunction for a depth
qapp85	apply Q operator
dpwig85	display output of wig85
glefil85	filter seismograms
gleins85	apply/remove instrument response
glemix85	merge seismograms
glespec85	spectra plot from time history
gle1085	generate 10 greens functions for VOL V programs
supfft	FFT for unlimited data points

VOLUME IV - SURFACE WAVE INVERSION

match	Phase matched Filter	
surf	Inversion Program	PC
srfedt	Edit surf(IV) dispersion file	
xspgam	interstation gamma	
xsprat	interstation Green's function	
xspthe	VOLIII synthetics -> VOLIV format	
dgplt	plot observed/theo dispersion	PC
vqplt	plot inverted vel/Q resolution	PC

VOLUME V - Cagniard de Hoop / Trace programs

accel	derivative of time history
delay	time delay of time history
dslqss	halfspace Green's functions (L. Johnson)
dsplot10	display 10 Green's functions
genray85	layered halfspace Green's functions (Langston)
instr	apply instrument response
integ	integrate time history
mech	apply focal mechanism to Green's functions
plot3	plot 3 component time histories
pulse	apply source pulse to Cagniard output
rhr10	plot 10 green's functions
bfilt	Butterworth filter Green's functions

VOLUME VI - FULL WAVENUMBER INTEGRATION

cspec8	Examine output of hspec8
dspec8	Data setup
fpplot	Plot G(f,p)
hspec8	Compute G(f,k)
hspec9	Compute G(f,r) directly
hspecp	Compute G(f,p)
kfplot	Plot G(f,k)
mrhwvinta	Compute G(f,r)
pltmod	Plot velocity model
ranmod	Generate random velocity model
refplt	Plot theoretical r-t travel times
rhfoc10	put Green's functions into VOLV format
rhlook	Examine G(f,k)
rhrprof	Plot G(r,t)
rhvwinta	G(f,r) from G(f,k)
shspec8	G(f,k) in oscillating medium

shspeep	G(f,p) in oscillating medium
tauplt	plot tau-p curves
tpplot	plot p-tau traces
whotheo	G(f,r) for wholespace
whospc	G(f,k) for wholespace
transiso	G(f,r) for transverse anisotropic medium
transiso8	G(f,k) for transverse anisotropic medium
dtraniso	data setup for traniso8

DISTRIBUTION LIST

Professor Keiti Aki
Center for Earth Sciences
University of Southern California
University Park
Los Angeles, CA 90089-0741

Professor Charles B. Archambeau
Cooperative Institute for Resch
in Environmental Sciences
University of Colorado
Boulder, CO 80309

Dr. Thomas C. Bache Jr.
Science Applications Int'l Corp.
10210 Campus Point Drive
San Diego, CA 92121 (2 copies)

Dr. Douglas R. Baumgardt
Signal Analysis & Systems Div.
ENSCO, Inc.
5400 Port Royal Road
Springfield, VA 22151-2388

Dr. S. Bratt
Science Applications Int'l Corp.
10210 Campus Point Drive
San Diego, CA 92121

Dr. Lawrence J. Burdick
Woodward-Clyde Consultants
P.O. Box 93245
Pasadena, CA 91109-3245 (2 copies)

Professor Robert W. Clayton
Seismological Laboratory/Div. of
Geological & Planetary Sciences
California Institute of Technology
Pasadena, CA 91125

Dr Karl Cogan
N. E. Research
P.O. Box 857
Norwich, VT 05055

Dr. Vernon F. Cormier
Department of Geology & Geophysics
U-45, Room 207
The University of Connecticut
Storrs, Connecticut 06268

Dr. Zoltan A. Der
ENSCO, Inc.
5400 Port Royal Road
Springfield, VA 22151-2388

Professor John Ferguson
Center for Lithospheric Studies
The University of Texas at Dallas
P.O. Box 830688
Richardson, TX 75083-0688

Professor Stanley Flatte'
Applied Sciences Building
University of California, Santa Cruz
Santa Cruz, CA 95064

Professor Steven Grand
Department of Geology
245 Natural History Building
1301 West Green Street
Urbana, IL 61801

Professor Roy Greenfield
Geosciences Department
403 Deike Building
The Pennsylvania State University
University Park, PA 16802

Professor David G. Harkrider
Seismological Laboratory
Div of Geological & Planetary Sciences
California Institute of Technology
Pasadena, CA 91125

Professor Donald V. Helmberger
Seismological Laboratory
Div of Geological & Planetary Sciences
California Institute of Technology
Pasadena, CA 91125

Professor Eugene Herrin
Institute for the Study of Earth
& Man/Geophysical Laboratory
Southern Methodist University
Dallas, TX 75275

Professor Robert B. Herrmann
Department of Earth & Atmospheric
Sciences
Saint Louis University
Saint Louis, MO 63156

Professor Lane R. Johnson
Seismographic Station
University of California
Berkeley, CA 94720

Professor Thomas H. Jordan
Department of Earth, Atmospheric
and Planetary Sciences
Mass Institute of Technology
Cambridge, MA 02139

Dr Alan Katka
Department of Geology &
Geophysics
Boston College
Chestnut Hill, MA 02167

Professor Leon Knopoff
University of California
Institute of Geophysics
& Planetary Physics
Los Angeles, CA 90024

Professor Charles A. Langston
Geosciences Department
403 Deike Building
The Pennsylvania State University
University Park, PA 16802

Professor Thorne Lay
Department of Geological Sciences
1006 C.C. Little Building
University of Michigan
Ann Harbor, MI 48109-1063

Dr. Randolph Martin III
New England Research, Inc.
P.O. Box 857
Norwich, VT 05055

Dr. Gary McCartor
Mission Research Corp.
735 State Street
P.O. Drawer 719
Santa Barbara, CA 93102 (2 copies)

Professor Thomas V. McEvilly
Seismographic Station
University of California
Berkeley, CA 94720

Dr. Keith L. McLaughlin
S-CUBED,
A Division of Maxwell Laboratory
P.O. Box 1620
La Jolla, CA 92038-1620

Professor William Menke
Lamont-Doherty Geological Observatory
of Columbia University
Palisades, NY 10964

Professor Brian J. Mitchell
Department of Earth & Atmospheric
Sciences
Saint Louis University
Saint Louis, MO 63156

Mr. Jack Murphy
S-CUBED
A Division of Maxwell Laboratory
11800 Sunrise Valley Drive
Suite 1212
Reston, VA 22091 (2 copies)

Professor J. A. Orcutt
Institute of Geophysics and Planetary
Physics, A-205
Scripps Institute of Oceanography
Univ. of California, San Diego
La Jolla, CA 92093

Professor Keith Priestley
University of Nevada
Mackay School of Mines
Reno, NV 89557

Wilmer Rivers
Teledyne Geotech
314 Montgomery Street
Alexandria, VA 22314

Professor Charles G. Sammis
Center for Earth Sciences
University of Southern California
University Park
Los Angeles, CA 90089-0741

Dr. Jeffrey L. Stevens
S-CUBED,
A Division of Maxwell Laboratory
P.O. Box 1620
La Jolla, CA 92038-1620

Professor Brian Stump
Institute for the Study of Earth & Man
Geophysical Laboratory
Southern Methodist University
Dallas, TX 75275

Professor Ta-liang Teng
Center for Earth Sciences
University of Southern California
University Park
Los Angeles, CA 90089-0741

Professor M. Nafi Toksoz
Earth Resources Lab
Dept of Earth, Atmospheric and
Planetary Sciences
Massachusetts Institute of Technology
42 Carleton Street
Cambridge, MA 02142

Professor Terry C. Wallace
Department of Geosciences
Building #11
University of Arizona
Tucson, AZ 85721

Weidlinger Associates
ATTN: Dr. Gregory Wojcik
620 Hansen Way, Suite 100
Palo Alto, CA 94304
Professor Francis T. Wu
Department of Geological Sciences
State University of New York
At Binghamton
Vestal, NY 13901

OTHERS (United States)

Dr. Monem Abdel-Gawad
Rockwell Internat'l Science Center
1049 Camino Dos Rios
Thousand Oaks, CA 91360

Professor Shelton S. Alexander
Geosciences Department
403 Deike Building
The Pennsylvania State University
University Park, PA 16802

Dr. Ralph Archuleta
Department of Geological
Sciences
Univ. of California at
Santa Barbara
Santa Barbara, CA

Dr. Muawia Barazangi
Geological Sciences
Cornell University
Ithaca, NY 14853

J. Barker
Department of Geological Sciences
State University of New York
at Binghamton
Vestal, NY 13901

Mr. William J. Best
907 Westwood Drive
Vienna, VA 22180

Dr. N. Biswas
Geophysical Institute
University of Alaska
Fairbanks, AK 99701

Dr. G. A. Bollinger
Department of Geological Sciences
Virginia Polytechnical Institute
21044 Derring Hall
Blacksburg, VA 24061

Dr. James Bulau
Rockwell Int'l Science Center
1049 Camino Dos Rios
P.O. Box 1085
Thousand Oaks, CA 91360

Mr. Roy Burger
1221 Serry Rd.
Schenectady, NY 12309

Dr. Robert Burridge
Schlumberger-Doll Resch Ctr.
Old Quarry Road
Ridgefield, CT 06877

Science Horizons, Inc.
ATTN: Dr. Theodore Cherry
710 Encinitas Blvd., Suite 101
Encinitas, CA 92024 (2 copies)

Professor Jon F. Claerbout
Professor Amos Nur
Dept. of Geophysics
Stanford University
Stanford, CA 94305 (2 copies)

Dr. Anton W. Dainty
AFGL/LWH
Hanscom AFB, MA 01731

Dr. Steven Day
Dept. of Geological Sciences
San Diego State U.
San Diego, CA 92182

Professor Adam Dziewonski
Hoffman Laboratory
Harvard University
20 Oxford St.
Cambridge, MA 02138

Professor John Ebel
Dept of Geology & Geophysics
Boston College
Chestnut Hill, MA 02167

Dr. Alexander Florence
SRI International
333 Ravenswood Avenue
Menlo Park, CA 94025-3493

Dr. Donald Forsyth
Dept. of Geological Sciences
Brown University
Providence, RI 02912

Dr. Anthony Gangi
Texas A&M University
Department of Geophysics
College Station, TX 77843

Dr. Freeman Gilbert
Institute of Geophysics &
Planetary Physics
Univ. of California, San Diego
P.O. Box 109
La Jolla, CA 92037

Mr. Edward Giller
Pacific Seirra Research Corp.
1401 Wilson Boulevard
Arlington, VA 22209

Dr. Jeffrey W. Given
Sierra Geophysics
11255 Kirkland Way
Kirkland, WA 98033

Dr. Henry L. Gray
Associate Dean of Dedman College
Department of Statistical Sciences
Southern Methodist University
Dallas, TX 75275

Rong Song Jih
Teledyne Geotech
314 Montgomery Street
Alexandria, Virginia 22314

Professor F.K. Lamb
University of Illinois at
Urbana-Champaign
Department of Physics
1110 West Green Street
Urbana, IL 61801

Dr. Arthur Lerner-Lam
Lamont-Doherty Geological Observatory
of Columbia University
Palisades, NY 10964

Dr. L. Timothy Long
School of Geophysical Sciences
Georgia Institute of Technology
Atlanta, GA 30332

Dr. Peter Malin
University of California at Santa Barbara
Institute for Central Studies
Santa Barbara, CA 93106

Dr. George R. Mellman
Sierra Geophysics
11255 Kirkland Way
Kirkland, WA 98033

Dr. Bernard Minster
Institute of Geophysics and Planetary
Physics, A-205
Scripps Institute of Oceanography
Univ. of California, San Diego
La Jolla, CA 92093

Professor John Nabelek
College of Oceanography
Oregon State University
Corvallis, OR 97331

Dr. Geza Nagy
U. California, San Diego
Dept of Ames, M.S. 8-010
La Jolla, CA 92093

Dr. Jack Oliver
Department of Geology
Cornell University
Ithaca, NY 14850

Dr. Robert Phinney/Dr. F.A. Dahlen
Dept of Geological
Geophysical Sci. University
Princeton University
Princeton, NJ 08540 (2 copies)

RADIX Systems, Inc.
Attn: Dr. Jay Pulli
2 Taft Court, Suite 203
Rockville, Maryland 20850

Professor Paul G. Richards
Lamont-Doherty Geological
Observatory of Columbia Univ.
Palisades, NY 10964

Dr. Norton Rimer
S-CUBED
A Division of Maxwell Laboratory
P.O. 1620
La Jolla, CA 92038-1620

Professor Larry J. Ruff
Department of Geological Sciences
1006 C.C. Little Building
University of Michigan
Ann Arbor, MI 48109-1063

Dr. Alan S. Ryall, Jr.
Center of Seismic Studies
1300 North 17th Street
Suite 1450
Arlington, VA 22209-2308 (4 copies)

Dr. Richard Sailor
TASC Inc.
55 Walkers Brook Drive
Reading, MA 01867

Thomas J. Sereno, Jr.
Service Application Int'l Corp.
10210 Campus Point Drive
San Diego, CA 92121

Dr. David G. Simpson
Lamont-Doherty Geological Observ.
of Columbia University
Palisades, NY 10964

Dr. Bob Smith
Department of Geophysics
University of Utah
1400 East 2nd South
Salt Lake City, UT 84112

Dr. S. W. Smith
Geophysics Program
University of Washington
Seattle, WA 98195

Dr. Stewart Smith
IRIS Inc.
1616 N. Fort Myer Drive
Suite 1440
Arlington, VA 22209

Rondout Associates
ATTN: Dr. George Sutton,
Dr. Jerry Carter, Dr. Paul Pomeroy
P.O. Box 224
Stone Ridge, NY 12484 (4 copies)

Dr. L. Sykes
Lamont Doherty Geological Observ.
Columbia University
Palisades, NY 10964

Dr. Pradeep Talwani
Department of Geological Sciences
University of South Carolina
Columbia, SC 29208

Dr. R. B. Tittmann
Rockwell International Science Center
1049 Camino Dos Rios
P.O. Box 1085
Thousand Oaks, CA 91360

Professor John H. Woodhouse
Hoffman Laboratory
Harvard University
20 Oxford St.
Cambridge, MA 02138

Dr. Gregory B. Young
ENSCO, Inc.
5400 Port Royal Road
Springfield, VA 22151-2388

OTHERS (FOREIGN)

Dr. Peter Basham
Earth Physics Branch
Geological Survey of Canada
1 Observatory Crescent
Ottawa, Ontario
CANADA K1A 0Y3

Dr. Eduard Berg
Institute of Geophysics
University of Hawaii
Honolulu, HI 96822

Dr. Michel Bouchon - Universite
Scientifique et Medicale de Grenob
Lab de Geophysique - Interne et
Tectonophysique - I.R.I.G.M.-B.P.
38402 St. Martin D'Herès
Cedex FRANCE

Dr. Hilmar Bungum/NTNF/NORSAR
P.O. Box 51
Norwegian Council of Science,
Industry and Research, NORSAR
N-2007 Kjeller, NORWAY

Dr. Michel Campillo
I.R.I.G.M.-B.P. 68
38402 St. Martin D'Herès
Cedex, FRANCE

Dr. Kin-Yip Chun
Geophysics Division
Physics Department
University of Toronto
Ontario, CANADA M5S 1A7

Dr. Alan Douglas
Ministry of Defense
Blacknest, Brimpton,
Reading RG7-4RS
UNITED KINGDOM

Dr. Manfred Henger
Fed. Inst. For Geosciences & Nat'l Res.
Postfach 510153
D-3000 Hannover 51
FEDERAL REPUBLIC OF GERMANY

Dr. E. Husebye
NTNF/NORSAR
P.O. Box 51
N-2007 Kjeller, NORWAY

Ms. Eva Johannisson
Senior Research Officer
National Defense Research Inst.
P.O. Box 27322
S-102 54 Stockholm
SWEDEN

Tormod Kvaerna
NTNF/NORSAR
P.O. Box 51
N-2007 Kjeller, NORWAY

Mr. Peter Marshall, Procurement
Executive, Ministry of Defense
Blacknest, Brimpton,
Reading FG7-4RS
UNITED KINGDOM (3 copies)

Dr. Ben Menaheim
Weizman Institute of Science
Rehovot, ISRAEL 951729

Dr. Svein Mykkeltveit
NTNF/NORSAR
P.O. Box 51
N-2007 Kjeller, NORWAY (3 copies)

Dr. Robert North
Geophysics Division
Geological Survey of Canada
1 Observatory crescent
Ottawa, Ontario
CANADA, K1A 0Y3

Dr. Frode Ringdal
NTNF/NORSAR
P.O. Box 51
N-2007 Kjeller, NORWAY

Dr. Jorg Schlittenhardt
Federal Inst. for Geosciences & Nat'l Res.
Postfach 510153
D-3000 Hannover 51
FEDERAL REPUBLIC OF GERMANY

University of Hawaii
Institute of Geophysics
ATTN: Dr. Daniel Walker
Honolulu, HI 96822

FOREIGN CONTRACTORS

Dr. Ramon Cabre, S.J.
c/o Mr. Ralph Buck
Economic Consular
American Embassy
APO Miami, Florida 34032

Professor Peter Harjes
Institute for Geophysik
Rhur University/Bochum
P.O. Box 102148, 4630 Bochum 1
FEDERAL REPUBLIC OF GERMANY

Professor Brian L.N. Kennett
Research School of Earth Sciences
Institute of Advanced Studies
G.P.O. Box 4
Canberra 2601
AUSTRALIA

Dr. B. Massinon
Societe Radiomana
27, Rue Claude Bernard
7,005, Paris, FRANCE (2 copies)

Dr. Pierre Mechler
Societe Radiomana
27, Rue Claude Bernard
75005, Paris, FRANCE

GOVERNMENT

Dr. Ralph Alewine III
DARPA/NMRO
1400 Wilson Boulevard
Arlington, VA 22209-2308

Dr. Robert Blandford
DARPA/NMRO
1400 Wilson Boulevard
Arlington, VA 22209-2308

Sandia National Laboratory
ATTN: Dr. H. B. Durham
Albuquerque, NM 87185

Dr. Jack Evernden
USGS-Earthquake Studies
345 Middlefield Road
Menlo Park, CA 94025

U.S. Geological Survey
ATTN: Dr. T. Hanks
Nat'l Earthquake Resch Center
345 Middlefield Road
Menlo Park, CA 94025

Dr. James Hannon
Lawrence Livermore Nat'l Lab.
P.O. Box 808
Livermore, CA 94550

U.S. Arms Control & Disarm. Agency
ATTN: Dick Morrow
Washington, D.C. 20451

Paul Johnson
ESS-4, Mail Stop J979
Los Alamos National Laboratory
Los Alamos, NM 87545

Ms. Ann Kerr
DARPA/NMRO
1400 Wilson Boulevard
Arlington, VA 22209-2308

Dr. Max Koontz
US Dept of Energy/DP 331
Forrestal Building
1000 Independence Ave.
Washington, D.C. 20585

Dr. W. H. K. Lee
USGS
Office of Earthquakes, Volcanoes,
& Engineering
Branch of Seismology
345 Middlefield Rd
Menlo Park, CA 94025

Dr. William Leith
USGS
Mail Stop 928
Reston, VA 22092

Dr. Richard Lewis
Dir. Earthquake Engineering and
Geophysics
U.S. Army Corps of Engineers
Box 631
Vicksburg, MS 39180

Dr. Robert Masse'
Box 25046, Mail Stop 967
Denver Federal Center
Denver, Colorado 80225

R. Morrow
ACDA/VI
Room 5741
320 21st Street N.W.
Washington, D.C. 20451

Dr. Keith K. Nakanishi
Lawrence Livermore National Laboratory
P.O. Box 808, L-205
Livermore, CA 94550 (2 copies)

Dr. Carl Newton
Los Alamos National Lab.
P.O. Box 1663
Mail Stop C335, Group E553
Los Alamos, NM 87545

Dr. Kenneth H. Olsen
Los Alamos Scientific Lab.
Post Office Box 1663
Los Alamos, NM 87545

Howard J. Patton
Lawrence Livermore National Laboratory
P.O. Box 808, L-205
Livermore, CA 94550

Mr. Chris Paine
Office of Senator Kennedy
SR 315
United States Senate
Washington, D.C. 20510

AFGL/LW
Hanscom AFB, MA 01731-5000

DARPA/PM
1400 Wilson Boulevard
Arlington, VA 22209

Defense Technical
Information Center
Cameron Station
Alexandria, VA 22314
(5 copies)

Defense Intelligence Agency
Directorate for Scientific &
Technical Intelligence
Washington, D.C. 20301

Defense Nuclear Agency/SPSS
ATTN: Dr. Michael Shore
6801 Telegraph Road
Alexandria, VA 22310

AFTAC/CA (STINFO)
Patrick AFB, FL 32925-6001

Dr. Gregory van der Vink
Congress of the United States
Office of Technology Assessment
Washington, D.C. 20510

Mr. Alfred Lieberman
ACDA/VI-OA' State Department Building
Room 5726
320 - 21st Street, NW
Washington, D.C. 20451

AFOSR/MP
ATTN: Colonel Jerry J. Perrizo
Bldg 410
Bolling AFB, Wash D.C. 20332-6448

HQ AFTAC/TT
Attn: Dr. Frank F. Pilotte
Patrick AFB, Florida 32925-6001

Mr. Jack Rachlin
USGS - Geology, Rm 3 C136
Mail Stop 928 National Center
Reston, VA 22092

Robert Reinke
AFWL/NTESG
Kirtland AFB, NM 87117-6008

HQ AFTAC/TGR
Attn: Dr. George H. Rothe
Patrick AFB, Florida 32925-6001

Donald L. Springer
Lawrence Livermore National Laboratory
P.O. Box 808, L-205
Livermore, CA 94550

Dr. Lawrence Turnbull
OSWR/NED
Central Intelligence Agency
CIA, Room 5G48
Washington, D.C. 20505

Dr. Thomas Weaver
Los Alamos Scientific Laboratory
Los Alamos, NM 97544

AFGL/SULL
Research Library
Hanscom AFB, MA 01731-5000 (2 copies)

Secretary of the Air Force (SAFRD)
Washington, DC 20330
Office of the Secretary Defense
DDR & E
Washington, DC 20330

HQ DNA
ATTN: Technical Library
Washington, DC 20305

Director, Technical Information
DARPA
1400 Wilson Blvd.
Arlington, VA 22209

AFGL/XO
Hanscom AFB, MA 01731-5000